

Centrality dependence of charged-neutral particle fluctuations in 158-A GeV $^{208}\text{Pb}+^{208}\text{Pb}$ collisions

M.M. Aggarwal,¹ Z. Ahammed,² A.L.S. Angelis,³ V. Antonenko,⁴ V. Arefiev,⁵ V. Astakhov,⁵ V. Avdeitchikov,⁵ T.C. Awes,⁶ P.V.K.S. Baba,⁷ S.K. Badyal,⁷ S. Bathe,⁸ B. Batiounia,⁵ T. Bernier,⁹ K.B. Bhalla,¹⁰ V.S. Bhatia,¹ C. Blume,⁸ D. Bucher,⁸ H. Büsching,⁸ L. Carlén,¹¹ S. Chattopadhyay,² M.P. Decowski,¹² H. Delagrange,⁹ P. Donni,³ M.R. Dutta Majumdar,² K. El Chenawi,¹¹ A.K. Dubey,¹³ K. Enosawa,¹⁴ S. Fokin,⁴ V. Frolov,⁵ M.S. Ganti,² S. Garpman,¹¹ O. Gavrishchuk,⁵ F.J.M. Geurts,¹⁵ T.K. Ghosh,¹⁶ R. Glasow,⁸ B. Guskov,⁵ H. Å.Gustafsson,¹¹ H. H.Gutbrod,¹⁷ I. Hrivnacova,¹⁸ M. Ippolitov,⁴ H. Kalechofsky,³ K. Karadjev,⁴ K. Karpio,¹⁹ B. W. Kolb,¹⁷ I. Kosarev,⁵ I. Koutcheryaev,⁴ A. Kugler,¹⁸ P. Kulinich,¹² M. Kurata,¹⁴ A. Lebedev,⁴ H. Löhner,¹⁶ L. Luquin,⁹ D.P. Mahapatra,¹³ V. Manko,⁴ M. Martin,³ G. Martínez,⁹ A. Maximov,⁵ Y. Miake,¹⁴ G.C. Mishra,¹³ B. Mohanty,^{2,13} M.-J. Mora,⁹ D. Morrison,²⁰ T. Mukhanova,⁴ D. S. Mukhopadhyay,² H. Naef,³ B. K. Nandi,¹³ S. K. Nayak,⁷ T. K. Nayak,² A. Nianine,⁴ V. Nikitine,⁵ S. Nikolaev,⁵ P. Nilsson,¹¹ S. Nishimura,¹⁴ P. Nomokonov,⁵ J. Nystrand,¹¹ A. Oskarsson,¹¹ I. Otterlund,¹¹ T. Peitzmann,¹⁶ D. Peressounko,⁴ V. Petracek,¹⁸ W. Pinganaud,⁹ F. Plasil,⁶ M.L. Purschke,¹⁷ J. Rak,¹⁸ R. Raniwala,¹⁰ S. Raniwala,¹⁰ N.K. Rao,⁷ F. Retiere,⁹ K. Reygers,¹⁶ G. Roland,¹² L. Rosselet,³ I. Roufanov,⁵ C. Roy,⁹ J.M. Rubio,³ S.S. Sambyal,⁷ R. Santo,⁸ S. Sato,¹⁴ H. Schlagheck,⁸ H.-R. Schmidt,¹⁷ Y. Schutz,⁹ G. Shabratova,⁵ T.H. Shah,⁷ I. Sibiriak,⁴ T. Siemiarczuk,¹⁹ D. Silvermyr,¹¹ B.C. Sinha,² N. Slavine,⁵ K. Söderström,¹¹ G. Sood,¹ S.P. Sørensen,²⁰ P. Stankus,⁶ G. Stefanek,¹⁹ P. Steinberg,¹² E. Stenlund,¹¹ M. Sumbera,¹⁸ T. Svensson,¹¹ A. Tsvetkov,⁴ L. Tykarski,¹⁹ E.C.v.d. Pijll,¹⁵ N.v. Eijndhoven,¹⁵ G.J.v. Nieuwenhuizen,¹² A. Vinogradov,⁴ Y.P. Viyogi,² A. Vodopianov,⁵ S. Vörös,³ B. Wyslouch,¹² G.R. Young⁶

(WA98 Collaboration)

¹ University of Panjab, Chandigarh 160014, India

² Variable Energy Cyclotron Centre, Calcutta 700064, India

³ University of Geneva, CH-1211 Geneva 4, Switzerland

⁴ RRC “Kurchatov Institute”, RU-123182 Moscow

⁵ Joint Institute for Nuclear Research, RU-141980 Dubna, Russia

⁶ Oak Ridge National Laboratory, Oak Ridge, Tennessee 37831-6372, USA

⁷ University of Jammu, Jammu 180001, India

⁸ University of Münster, D-48149 Münster, Germany

⁹ SUBATECH, Ecole des Mines, Nantes, France

¹⁰ University of Rajasthan, Jaipur 302004, Rajasthan, India

¹¹ University of Lund, SE-221 00 Lund, Sweden

¹² MIT Cambridge, MA 02139

¹³ Institute of Physics, Bhubaneswar 751005, India

¹⁴ University of Tsukuba, Ibaraki 305, Japan

¹⁵ Universiteit Utrecht/NIKHEF, NL-3508 TA Utrecht, The Netherlands

¹⁶ KVI, University of Groningen, NL-9747 AA Groningen, The Netherlands

¹⁷ Gesellschaft für Schwerionenforschung (GSI), D-64220 Darmstadt, Germany

¹⁸ Nuclear Physics Institute, CZ-250 68 Rez, Czech Rep.

¹⁹ Institute for Nuclear Studies, 00-681 Warsaw, Poland and

²⁰ University of Tennessee, Knoxville, Tennessee 37966, USA

(Dated: April 22, 2019)

Results on the study of localized fluctuations in the multiplicity of charged particles and photons produced in 158-A GeV/c Pb+Pb collisions are presented for four different centrality classes. The charged versus neutral particle multiplicity correlations in common phase space regions of varying azimuthal size are analyzed by two different methods. Various types of mixed events are constructed to probe fluctuations arising from different sources. The measured results are compared to those from simulations and from mixed events. The comparison indicates the presence of non-statistical fluctuations in both the charged particle and photon multiplicities in limited azimuthal regions which decrease with decrease in centrality. However, no correlated charged-neutral fluctuations, a possible signature of formation of disoriented chiral condensates, are observed. An upper limit on the production of disoriented chiral condensates has been set.

PACS numbers: 25.75.+r,13.40.-f,24.90.+p

I. INTRODUCTION

Synchrotron (SPS) and the Relativistic Heavy-Ion

The large number of particles produced in relativistic heavy-ion collisions at the Super Proton

Collider (RHIC) provide an opportunity to analyze and study, on an event-by-event basis, fluctuations in physical observables, such as particle multiplicities, transverse momenta, and their correlations. These studies provide information on the dynamics of multiparticle production and may help to reveal the phase transition from hadronic matter to quark-gluon plasma (QGP) [1, 2]. The formation of hot and dense matter in high energy heavy-ion collisions also has the possibility to create matter in a chiral symmetry restored phase in the laboratory. After the initial stage of the collision, the system cools and expands returning to the normal QCD vacuum in which chiral symmetry is spontaneously broken. During this process, a metastable state may be formed in which the chiral condensate is disoriented from the true vacuum direction. This transient state would subsequently decay by emitting pions coherently within finite subvolumes or domains of the collision region. The possibility of formation of disoriented chiral condensate (DCC) has been discussed extensively in recent years [3, 4, 5, 6, 7, 8, 9, 10, 11]. The detection and study of the DCC state would provide valuable information about the chiral phase transition and the vacuum structure of strong interactions.

Theoretical studies [5, 6, 7] suggest that isospin fluctuations caused by formation of a DCC would produce clusters of coherent pions in localized phase space domains. The formation of DCC domains would be associated with large event-by-event fluctuations in the ratio of neutral to charged pions. The probability distribution of the neutral pion fraction, f , in such a DCC domain has been shown [3] to follow the relation:

$$P(f) = \frac{1}{2\sqrt{f}} \quad \text{where} \quad f = N_{\pi^0}/N_{\pi} \quad (1)$$

which is quite different from that of the normal pion production mechanism. For the normal pion production, where the production of π^0, π^+, π^- are equally probable, the f distribution is binomial peaking at $1/3$.

In the experimental search for localized domains of DCC a practical approach is to search for events with large and localized fluctuations in the ratio of the number of photons to charged particles which would directly reflect fluctuations in the neutral to charged pion ratio. Typical event structures would be similar to the Centauro and anti-Centauro events reported by the JACEE collaboration [12]. Results from other cosmic ray experiments have not ruled out the possibility of the DCC formation mechanism [13]. The accelerator based studies carried out in $p - \bar{p}$ [14] and heavy ion [15, 16] reactions have investigated particle production over extended regions of phase space. These analyses were not sensitive to

the presence of small domains of DCC localized in phase space. A first search for evidence of localized domains of DCC has been carried out at the SPS by the WA98 experiment in a detailed study of central Pb+Pb events [17]. The analysis showed the presence of localized non-statistical fluctuations in the multiplicity of both photons and charged particles. However, the charged-neutral fluctuations were found not to be correlated event-by-event, as would be expected for a DCC production mechanism. An upper limit on the frequency of DCC formation in central Pb+Pb collisions was set. Recently there have been theoretical suggestions to look for DCC formation in events of intermediate centralities [18]. In this paper we present first results on the centrality dependence of localized charged-neutral multiplicity fluctuations. It is based on an analysis of event-by-event fluctuation in the relative number of charged particles and photons detected within the common acceptance of the photon and charged particle multiplicity detectors of the WA98 experiment [19].

The paper is organized in the following manner: In the next section we describe the detectors used for the present analysis, the centrality selection criteria, the data reduction, and simulation. Section III deals with the analysis techniques, where two analysis methods are presented, one based on the correlation of photons and charged particles, and the other based on a discrete wavelet transformation analysis. In section IV, we present in detail the construction of mixed events used for this study. Section V discusses the ability of the mixed events to probe specific fluctuations. Final results and discussion are given in section VI. A summary is presented in section VII.

II. EXPERIMENTAL SETUP AND DATA REDUCTION

In the WA98 experiment at CERN [19], the main emphasis has been on high precision, simultaneous detection of both hadrons and photons. The experimental setup consisted of large acceptance hadron and photon spectrometers, detectors for charged particle and photon multiplicity measurements, and calorimeters for transverse and forward energy measurements. The present study makes use of the data from the photon multiplicity detector (PMD), the silicon pad multiplicity detector (SPMD) and the mid-rapidity calorimeter (MIRAC).

A. Centrality Selection

The centrality of the interaction was determined from the total transverse energy (E_T) measured by the mid-rapidity calorimeter (MIRAC) [20]. The

MIRAC measures both the transverse electromagnetic (E_T^{em}) and hadronic (E_T^{had}) energies in the interval $3.5 \leq \eta \leq 5.5$ with a resolution of $17.9\%/\sqrt{E}$ and $46.1\%/\sqrt{E}$, respectively, where E is expressed in GeV. The centrality, or impact parameter of the collision, has a strong correlation with the amount of E_T produced. Events with large E_T production correspond to the most central, small impact parameter, collisions [21].

The centralities are expressed as fractions of the minimum bias cross section as a function of the measured total E_T . For the present analysis we have used data selections in four centrality bins, the top 5% (henceforth referred to as centrality-1), 5% - 10% (centrality-2), 15% - 30% (centrality-3), and 45% - 55% (centrality-4) of the minimum bias cross section. The minimum bias distribution of the total E_T is shown in Fig. 1. The centrality bins used in this analysis are marked in the figure.

B. Photon Multiplicity Detector

The photon multiplicity is measured using the preshower photon multiplicity detector (PMD) located at a distance of 21.5 meters from the target. The PMD consists of 3 radiation lengths (X_0) thick lead converter plates in front of an array of square scintillator pads of four sizes, varying from 15 mm×15 mm to 25 mm×25 mm, placed in 28 box modules. Each box module consists of a matrix of 38×50 scintillator pads read out using an image intensifier plus charged coupled device (CCD) camera system. The scintillation light is transmitted to the readout device via a short wavelength shifting fiber spliced to a long extra-mural absorber (EMA) coated clear fiber. The total light amplification of the readout system is ~ 40000 . Digitization of the CCD pixel charge is done by a set of custom built fast-bus modules employing an 8 bit 20 MHz Flash ADC system. Details of the design and characteristics of the PMD may be found in Ref. [22, 23]. The results presented here make use of the data from the central 22 box modules covering the pseudo-rapidity range of $2.9 \leq \eta \leq 4.2$. The clusters of hit pads, having total ADC content above a hadron rejection threshold are identified as photon-like, the multiplicity being denoted by $N_{\gamma\text{-like}}$. The photon counting efficiencies for the central to peripheral cases varies from 68% to 73%. The purity of the photon sample in the two cases varies from 65% to 54%. The acceptance in terms of transverse momentum (p_T) extends down to about 30 MeV/c, however the PMD energy resolution is not sufficient for particle-by-particle p_T measurement.

C. Silicon Pad Multiplicity Detector

The charged particle multiplicity (N_{ch}) is measured using the circular Silicon Pad Multiplicity Detector (SPMD) located 32.8 cm from the target and having full azimuthal coverage in the region $2.35 < \eta < 3.75$, corresponding to the central rapidity region at SPS energies (where $\eta_{CMS} = 2.92$). The detector consists of four overlapping quadrants, each fabricated from a single 300 μm thick silicon wafer. The active area of each quadrant is divided into 1012 pads forming 46 azimuthal wedges and 22 radial bins with a pad size increasing with radius to provide uniform pseudo-rapidity coverage. The efficiency for detection of a charged particle in the active area has been determined in test beam measurements to be better than 99 %. Conversely, the detector is transparent to high energy photons, since only about 0.2 % are expected to interact in the silicon. During the data recording, 95 % of the pads worked properly and are used in this analysis. Details of the characteristics of SPMD can be found in Ref. [15, 24].

D. Data Reduction

The data presented here were taken during December 1996 at the CERN SPS with the 158-A GeV Pb ion beam on a Pb target of thickness 213 μm . The WA98 Goliath magnet was switched off during these runs. Events with beam pile-up, downstream interactions, and pile-up in the CCD camera system were rejected in the off-line analysis [15, 23]. The data have been analyzed for the region of common η ($2.9 < \eta < 3.75$) and ϕ coverage of the SPMD charged particle and PMD photon multiplicity detectors. The $N_{\gamma\text{-like}}$ and the N_{ch} distributions for the four centrality bins are shown in Figs. 2 and 3. The mean number of photons and charged particles along with the root mean square deviations are shown in the figures.

The various sources of systematic errors associated with the $N_{\gamma\text{-like}}$ and N_{ch} distributions have been investigated and described in detail previously [23, 25]. These include:

- (a) The uncertainty in the energy calibration and the associated uncertainty in the energy threshold for hadron rejection in the PMD leads to an error in the efficiency for $N_{\gamma\text{-like}}$ clusters. The nominal hadron rejection threshold was set at three times the minimum ionizing particle (MIP) peak. The value of the threshold was reduced by 10% [23] in order to estimate the systematic error. The associated error in $N_{\gamma\text{-like}}$ is 2.5%.

- (b) The error due to the effect of clustering of pad signals in the PMD is a major source of error in $N_{\gamma\text{-like}}$. This error is determined from simulation by comparing the number of known tracks on the PMD with the total number of reconstructed photon-like clusters. It is found that the number of clusters exceeds the number of tracks by 3% in the case of peripheral events and by 7% for high multiplicity central events.
- (c) The error due to the variation in pad-to-pad gains of the scintillators in PMD was found to be less than 1%.
- (d) The uncertainty in the N_{ch} determination with the SPMD has been estimated to be about 4% [15].
- (e) The error due to the finite resolution in the measurement of the total transverse energy (E_T) in MIRAC [23] translates into an uncertainty in the centrality selection. The effect of this systematic error has been determined by performing the analysis with varying centrality cut within the MIRAC resolution.

The contribution of each of these various systematic errors to the final results are discussed in the following sections.

E. Simulated Events

Simulated events were generated using the VENUS 4.12 event generator [26] with the default parameter values. The output was processed through a detector simulation package in the GEANT 3.21 [27] framework. This simulation incorporated the full WA98 experimental setup. The effect of Landau fluctuations in the energy loss of charged particles in silicon was included in the SPMD simulation [15]. For the PMD simulation, the GEANT results in terms of energy deposition in pads were converted to the pad ADC values using the MeV-ADC calibration relation. After this the ADC distribution is convoluted with a Gaussian function of proper width taken from the readout resolution curve. If the energy deposition is less than 3 MIP, a Landau distribution is used for convolution. The details of the PMD simulations taking into account the detector and readout effects can be found in Ref. [22]. The centrality selection with the simulated data has been made in an identical manner to the data, determined from the simulated total transverse energy in MIRAC. The minimum bias total E_T distribution predicted by VENUS is shown by the dashed histogram in Fig. 1. The agreement with the data is seen to be quite reasonable. A total

of 60K VENUS events with simulated detector response were generated for the present study. These simulated events (henceforth referred to simply as VENUS events unless otherwise specified) were then processed with the same analysis codes as used for the analysis of the experimental data.

III. ANALYSIS TECHNIQUES

Two different analysis methods have been used in the present study. In the first analysis method, the magnitude of the $N_{\gamma\text{-like}}$ versus N_{ch} multiplicity fluctuations is obtained in decreasing phase space regions. The second method employed the discrete wavelet transformation technique to investigate the relative magnitude of the $N_{\gamma\text{-like}}$ versus N_{ch} fluctuations in adjacent phase space regions. The results from these methods of analysis applied to data, VENUS and various sets of mixed events (to be discussed later) are compared to draw proper conclusions.

A. N_{γ} versus N_{ch} correlations

In order to search for localized fluctuations in the photon and charged particle multiplicities, which may have non-statistical origin, the correlation between $N_{\gamma\text{-like}}$ and N_{ch} is investigated at various scales in η and ϕ .

The event-by-event correlation between $N_{\gamma\text{-like}}$ and N_{ch} has been studied in various ϕ -intervals by dividing the entire ϕ -space into 2, 4, 8, and 16 bins. The method of analysis is similar to that described in Ref. [15, 17]. Fig. 4 shows scatter plot of the correlation between $N_{\gamma\text{-like}}$ and N_{ch} for the top centrality bin. The correlation plots for each ϕ interval size, including the case of the full interval with no segmentation, are shown. The distributions for the other three centrality bins are qualitatively similar. A common correlation axis (Z) has been obtained for the full distribution by fitting the $N_{\gamma\text{-like}}$ and N_{ch} correlation with a second order polynomial. The correlation axis with fit parameters are shown in the figures. The distances of separation (D_Z) between a data point and the correlation axis has been calculated with the convention that D_Z is positive for points below the Z -axis. The distribution of D_Z represents the relative fluctuations of $N_{\gamma\text{-like}}$ and N_{ch} from the correlation axis for any chosen ϕ bin size. In order to compare the fluctuations for different ϕ bins on a similar footing, a scaled variable, $S_Z = D_Z/s(D_Z)$, is used where $s(D_Z)$ represents the rms deviation of the D_Z distribution for VENUS events analyzed in the same manner. The D_Z distributions of data, mixed events and the sim-

ulated events for a given centrality and ϕ bin size are all scaled by the same $s(D_Z)$ corresponding to the VENUS events for the respective centrality and azimuthal bin size. The presence of events with localized fluctuations in $N_{\gamma\text{-like}}$ and N_{ch} , at a given ϕ bin, is expected to result in a broader distribution of S_Z compared to those for normal events. Comparing the rms deviations of the S_Z distributions of data, mixed events (to be discussed later), and VENUS events may allow to infer the presence of non-statistical localized fluctuations.

B. Multi-resolution DWT analysis

A multi-resolution analysis using discrete wavelet transformations (DWT) [28] has been shown to be quite powerful in the search for localized domains of DCC [29, 30, 31]. The beauty of the DWT technique lies in its power to analyze a spectrum at different resolutions with the ability to identify fluctuations present at any scale. This method has been utilized very successfully in many fields including image processing, data compression, turbulence, human vision, radar, and earthquake prediction [28].

For the present DWT analysis the full azimuthal region is divided into smaller bins in ϕ , the number of bins at a given scale j being 2^j . The input to the analysis is a spectrum of the sample function at the smallest bin in ϕ corresponding to the highest resolution scale, j_{max} . In the present case the sample function is chosen to be the photon fraction, given by:

$$f'(\phi) = N_{\gamma\text{-like}}(\phi)/(N_{\gamma\text{-like}}(\phi) + N_{\text{ch}}(\phi)) \quad (2)$$

A multi-resolution analysis has been carried out using $D-4$ wavelet basis on the above sample function starting with $j_{\text{max}} = 5$. It may be mentioned that there are several families of wavelet bases distinguished by the number of coefficients and the level of iteration, we have used the frequently employed $D-4$ wavelet basis [32]. The output of the DWT consists of a set of wavelet or father function coefficients (FFC) at each scale, from $j = 1, \dots, (j_{\text{max}} - 1)$. The coefficients obtained at a given scale, j , are derived from the distribution of the sample function at one higher scale, $j + 1$. The FFCs quantify the deviation of the bin-to-bin fluctuations in the sample function at that higher scale relative to the average behavior. The presence of localized non-statistical fluctuations will increase the rms deviation of the distribution of FFCs and may result in non-Gaussian tails [29, 31]. The DWT technique as used in this analysis has been demonstrated in our earlier publication [17]. Once again, comparing the rms deviations of the FFC distributions of data, mixed events,

and VENUS events may allow to infer the presence of localized fluctuations.

IV. CONSTRUCTION OF MIXED EVENTS

It is possible to search for non-statistical fluctuations in the experimental data in a model independent way by comparison of the data with mixed events generated from the data itself. Furthermore, it is necessary to isolate the various contributions to the fluctuations and to understand all detector related effects in the data. This has been done by generating different types of mixed events which preserve the global correlation between $N_{\gamma\text{-like}}$ and N_{ch} . Fluctuations in the ratio of N_{γ} to N_{ch} can arise due to fluctuations in N_{γ} only, fluctuations in N_{ch} only, or fluctuation in both N_{γ} and N_{ch} . Furthermore, the fluctuations in N_{γ} and N_{ch} may be correlated event-by-event, as nominally expected in the case of DCC formation. Each of these possibilities is investigated through the construction of four different kinds of mixed events. The method of construction of these mixed events and the type of fluctuations they probe are described next.

A. Maximally Mixed Events

The first set of mixed events, referred to as M1 events, are constructed to remove all correlations to the greatest extent possible to provide a baseline for comparison to the real event data. They were generated by mixing hits in both the photon and charged particle detectors separately but still satisfying the global $N_{\gamma\text{-like}}-N_{\text{ch}}$ correlation of the real event in the full acceptance. This means that on an event-by-event basis the total photon multiplicity and charged particle multiplicity of the mixed event were identical to those of the real event to which it corresponds. Thus, the scatter plot of the mixed events is identical to the real events for the single bin case shown in Fig. 4. The idea is to constrain the mixed events to be identical to real events globally and then compare them to the real data in localized regions of phase space to search for indications of non-statistical localized fluctuations in the data.

The M1 type of mixed events were constructed from the pool of all photon-like and charged particle hits, in which the hit position (η and ϕ) and event information (event number and total multiplicity) was kept for both the photon-like and charged particle hits. For a given real event measured to have multiplicities $N_{\gamma\text{-like}}$ and N_{ch} in the full acceptance region, a mixed event was constructed by randomly selecting $N_{\gamma\text{-like}}$ photon-like hits from the pool of photon-like hits and N_{ch} charged particle hits from

the pool of charged particle hits. This procedure was repeated for each real event. Care was taken such that no two hits from the same real event were used in the construction of a mixed event. Also, for the mixed events, hits within either the SPMD or PMD detector were not allowed to lie within the two-track resolution of that detector. In brief, the M1 mixed events randomly distribute the hits in each individual detector but keep the global correlation between the $N_{\gamma\text{-like}}$ and N_{ch} multiplicity. They provide a maximally randomized sample of PMD and SPMD hits. Comparisons of such mixed events to real events will be most sensitive to the presence of localized fluctuations. However, in themselves they would not isolate the source of fluctuations as being due to N_{γ} and/or N_{ch} , or correlations between N_{γ} and N_{ch} .

B. Minimally Mixed Events

A second type of mixed events, referred to as M2 mixed events, were constructed to investigate the presence of correlated event-by-event fluctuations between N_{γ} and N_{ch} . These mixed events had a minimal amount of randomization since they were generated by mixing the photon hits taken unaltered from one event with the charged particle hits taken unmodified from another event. As with the M1 mixed events, the global (bin 1) $N_{\gamma\text{-like}}-N_{\text{ch}}$ correlation was maintained to be exactly the same as the data. To construct such mixed events, for a given real event measured to have multiplicities $N_{\gamma\text{-like}}$ and N_{ch} in the full acceptance region, a mixed event was constructed by keeping the PMD $N_{\gamma\text{-like}}$ portion of the event intact, but combining it with the unaltered SPMD portion of a different randomly selected event, but constrained to have almost the same charged particle multiplicity N_{ch} . This procedure was repeated for each real event. In brief, this type of mixed event keeps the event-by-event hit structure in each detector identical to that in real events. Thus, such mixed events keep the individual localized fluctuations present in N_{γ} or N_{ch} , but remove the event-by-event localized correlated fluctuations between them. Comparison of such mixed events to real events may reveal the presence of correlated localized fluctuations between N_{γ} and N_{ch} .

C. Partially Mixed Events

Intermediate between the M1 and M2 types of mixed events are a third and fourth type of partially mixed event, referred to as M3- γ and M3-ch mixed events. These were constructed to provide information regarding the contribution to the localized

TABLE I: Type of fluctuations preserved by various mixed events

Fluctuation	Mixed		Event	
	M1	M2	M3-ch	M3- γ
N_{γ} -only	No	Yes	Yes	No
N_{ch} - only	No	Yes	No	Yes
correlated $N_{\gamma}-N_{\text{ch}}$	No	No	No	No

fluctuations in the N_{γ} to N_{ch} ratio from the individual observables (N_{γ} and N_{ch}). They were generated from real events by mixing hits in one of the detectors (following the procedure for construction of M1 mixed events) and keeping the hit structure of the event in the other detector intact. M3- γ mixed events correspond to the case where the hits within the photon detector are unaltered while the hits in the charged particle detector are mixed. Similarly in M3-ch mixed events the hits in the charged particle detector were unaltered and the hits in the photon detector were mixed. In each type of mixed event the global $N_{\gamma\text{-like}}-N_{\text{ch}}$ correlation is maintained as in the real event. The two track resolution in the detectors where the hits are mixed is kept identical to that in real events. The total number of mixed events is the same as the number of real events. Comparison of such mixed events to real events and the other types of mixed events will reveal the presence of localized fluctuations in N_{γ} or N_{ch} separately.

A summary of the different sources of fluctuations in the ratio of N_{γ} to N_{ch} probed by each of the types of mixed events is given in Table 1.

V. DEMONSTRATION OF ANALYSIS METHOD

To demonstrate the sensitivity of the analysis method, we have applied the DWT analysis to events generated using a simple DCC-like model. The analysis is applied to the “real” DCC events as well as the various types of mixed events described above. In this model, localized non-statistical $N_{\gamma}-N_{\text{ch}}$ fluctuations have been introduced into the output of the VENUS event generator. To implement the fluctuations, the final state pions within a localized $\eta-\phi$ region from VENUS are interchanged pairwise ($\pi^+\pi^- \leftrightarrow \pi^0\pi^0$) according to the DCC probability distribution given in Eq 1. The fluctuations were generated over a localized region of $\eta = 3 - 4$ and a ϕ interval of 90° . The π^0 's were then allowed to decay. The simple model used here results in an anti-correlation between N_{γ} and N_{ch} . It also results in non-statistical fluctuations in both N_{γ} and N_{ch} individually. Since the probability to produce events with localized charged-neutral fluctuations is

unknown, ensembles of events, here referred to as “nDCC events”, were produced as a mixture of normal events and events with localized fluctuations. The fraction of events with localized fluctuations in the nDCC sample was varied as a parameter to be studied.

The DWT analysis was carried out on an ensemble of nDCC events and their corresponding mixed event sets. By ensemble of nDCC events we mean sets of events having different percentages of events with localized fluctuations. The percentage varied from zero, with no localized fluctuations, to an event set where all events had localized charge-neutral fluctuations. For every nDCC event set the four set of mixed events (M1, M2, M3- γ , and M3-ch) were constructed and analyzed. The rms deviations of the FFC distributions for each set of nDCC events and corresponding mixed event sets were obtained. The results are plotted in Fig. 5 as a function of the percentage of localized DCC-type fluctuation events in the nDCC event set.

It is seen that the rms deviations of the FFC distributions of the nDCC events increase as the percentage of events with localized fluctuations in N_γ - N_{ch} increases. This is the expected behaviour and demonstrates the sensitivity of the DWT technique to identify fluctuations. On the other hand, the rms deviations of the FFC distributions of the M1 type events are found to be independent of the percentage of events having localized fluctuations. This is also the expected behaviour and demonstrates that the M1 mixed events can be used as a model-independent baseline from which to deduce the presence of fluctuations. However, the deviation of the real events from the M1 mixed events does not give information about the relative contributions of the individual N_γ and N_{ch} fluctuations. The rms deviations of the FFC distributions of the M3 mixed events are found to be intermediate to those obtained for nDCC events and M1 mixed events. They indicate the separate contributions of the N_γ or N_{ch} fluctuations alone to the ratio. The rms deviations of the M2 mixed events are higher than those of M1 and M3 mixed events. That is because the M2 mixed events keep the separate contributions of both the N_γ and N_{ch} fluctuations. However, the rms deviations of the M2 mixed events are consistently below those for the nDCC events. This is because the M2 events randomize the correlations between N_γ and N_{ch} . The difference between the M2 mixed events and the nDCC events indicates the presence of the DCC-like correlated N_γ - N_{ch} fluctuations. The relative pattern of rms values for the real events and the various mixed events seen in Fig. 5 provides a rather unambiguous model-independent signature for DCC-like fluctuations.

For nDCC events with vanishing fraction of events with fluctuations, it is seen in Fig. 5 that the rms deviations of the FFC distributions for all types of mixed events are higher than those for the nDCC events. This is due to the presence of additional correlations between N_{ch} and $N_{\gamma\text{-like}}$. These are primarily due to the charged particle contamination in the $N_{\gamma\text{-like}}$ data sample, as well as residual correlations due to impact parameter (see Fig. 4), which are removed by the event mixing procedure and thereby results in larger rms deviations for the mixed events. It may be mentioned that the effect of charged particle contamination on the above aspect has been studied in detail by varying the contamination in VENUS simulations and constructing VENUS mixed events [33]. It was observed that the rms deviations of FFC distribution of VENUS events were lower than the corresponding mixed events for various values of contamination. In order to take into account this effect, for comparison with real data all mixed event rms values have been rescaled by the percentage difference between the rms deviations of the VENUS distributions and those of the corresponding VENUS mixed events, as also discussed in Ref. [17]. For larger percentages of DCC-like events, the anti-correlation between N_{ch} and $N_{\gamma\text{-like}}$ overcomes the correlations between N_{ch} and $N_{\gamma\text{-like}}$ mostly due to the charged particle contamination in the $N_{\gamma\text{-like}}$ sample and hence the rms deviations of the FFC distributions of nDCC events is higher than those of the mixed events.

VI. RESULTS AND DISCUSSION

In the analysis of experimental data, the results from the measured data are compared with simulated and mixed events. Below we discuss the results obtained from such a comparison using two different analyses methods discussed earlier.

A. N_γ versus N_{ch} correlation results

The S_Z distributions calculated for different ϕ bin sizes are shown in Fig. 6 for data, M1, and VENUS events, for the four different centrality selections. The distributions for the other types of mixed events are not shown for clarity of presentation. The small differences in the S_Z distributions have been quantified in terms of the corresponding rms deviations, of these distributions shown in Fig. 7. The statistical errors on the values are small and are within the size of the symbols. The bars represent statistical and systematic errors added in quadrature. The various sources of systematic error have been discussed in an earlier section. An additional systematic error from

the fit errors associated with the determination of the correlation axis (Z) is also included. In general, the width of the S_Z distribution increases from the most central to less central event selections and decreases with decreasing bin size. The rms deviations of the S_Z distribution for VENUS events are equal to one for all centrality and all bins in ϕ by definition.

As seen in Fig. 7, the widths of the S_Z distributions for mixed events closely follow those of the data. The mixed events have been constructed such that the $N_{\gamma\text{-like}}$ vs. N_{ch} correlations are maintained for the full azimuth (bin 1), with the result that the rms deviations of data and mixed events are identical in this case by construction. Some correlations between N_{ch} and $N_{\gamma\text{-like}}$ are expected, mostly as a result of the charged particle contamination in the $N_{\gamma\text{-like}}$ data sample, but are removed by the event mixing procedure and thereby result in a small difference between the real and mixed events, as seen in the analysis of the VENUS events, discussed earlier. All of the mixed event S_Z distribution rms values (Fig. 7) have therefore been rescaled by the percentage difference between the rms deviations of the VENUS distributions and those of the corresponding VENUS mixed events for each centrality class (Ref. [17]). The rms deviations S_Z distributions of the M2 mixed events are found to agree with those of the experimental data within errors for all four centrality classes and for all azimuthal bin sizes. This indicates the absence of event-by-event localized correlated fluctuations in $N_{\gamma\text{-like}}$ and N_{ch} , such as would be expected for DCC-like fluctuations. On the other hand, the rms deviations of the M1 mixed events are found to be systematically lower than those of the data for 2, 4, and 8 bins in ϕ for centrality bins 1, 2, and 3. The results for both types of M3 mixed events are found to be intermediate between those of the data and the M1 mixed events. The results indicate the presence of localized fluctuations in the data in both the photon and charged particle multiplicities. For the case of the most peripheral centrality selection (centrality-4), the rms deviations of the S_Z distributions of data and the various mixed events are found to be in closer to each other within the quoted errors. The rms deviations for the VENUS simulated events are 1 for all bins in azimuth by definition of S_Z and are significantly different than the measured results.

B. Multi-resolution DWT analysis results

The FFC distributions, at scales $j=1$ to 4, corresponding to 4 to 32 bins in azimuthal angle, are shown in Fig. 8 for data, M1, and VENUS events for the four centrality classes. The results for other types of mixed events are not shown for clarity of

presentation. The widths of the FFC distributions are found to increase in going from the most central to most peripheral centrality class. The rms deviations of these FFC distributions are summarized in Fig. 9. Similar to the case for the S_Z distributions discussed above, the rms deviations of the mixed events have been rescaled by the percentage difference between the rms deviations of the VENUS FFC distributions and those of the VENUS mixed events for each centrality class. The statistical errors are small and are within the size of the symbols. The bars represent statistical and systematic errors added in quadrature.

The rms deviations of the FCC distributions for the data, VENUS, and mixed events are found to be close to each other (within quoted errors) for the case of 32 bins in ϕ for all of the four centrality classes. The rms deviations for the FFC distribution of M2 mixed events are found to closely follow those of the data for all centrality classes and all bins in ϕ , while the rms deviations for the M3 mixed events lie between those of the data and M1 mixed events. These results are consistent with those obtained from the analysis of the S_Z distributions. These observations indicate the absence of event-by-event localized correlated fluctuations (DCC-like) between $N_{\gamma\text{-like}}$ and N_{ch} . They also suggest the presence of localized fluctuations in both photons and charged particle multiplicities for intermediate bin sizes in azimuth. The rms values of the FFC distributions for VENUS events are close to those of the M1 mixed events for centrality classes 1, 2, and 3. However they are slightly higher for the most peripheral centrality class (centrality-4).

C. Discussion

The results from the two independent methods of analysis are consistent and indicate the absence of event-by-event correlated fluctuations in the photon and charged particle multiplicities. However they do suggest the presence of uncorrelated fluctuations in both the photon and charged particle multiplicities for intermediate bin sizes in ϕ . The data has been compared to various kinds of mixed events and to simulated events which take into account many detector related effects. Still it is worthwhile to explore the extent of other possible experimental effects which might affect the observed rms deviations of the S_Z and FFC distributions. As discussed extensively in Refs. [15, 22, 23], care has been taken during the data taking and during the data processing to closely monitor the performance of the PMD and SPMD. The detector uniformity of the PMD was studied in detail by using the minimum ionizing particle (MIP) signal from the data for all pads of the

22 boxes. The fluctuations of the pad-to-pad relative gains were approximately 10%. The gain corrections were made for each pad. Corrections for gain variations during the data taking period were made periodically for both the PMD and SPMD. This reduces the possibility of abrupt gain or threshold changes during the run period. Events with obvious detector readout effects, such as missing or dead regions, were carefully removed from the data sample. It should be recalled that most detector effects are reflected in the mixed events.

The effect of local fluctuations in the performance of the PMD has been studied using simulated VENUS events. In one test, the gain of a group of pads corresponding to one or more PMD cameras was randomly varied. A 30% change of gain in one camera for all events resulted in an increase of 0.7% in the rms deviations. Changing the gains of three cameras by 30% for all events resulted in an increase of the rms deviations by 1.7%. Because the camera gains were closely monitored online and during the processing of the data this is considered to be a highly unlikely scenario. Still, these changes are within the quoted errors of Figs. 7 and 9 which indicates that local gain and threshold variations would not account for the observed differences between the data and the M1 mixed events.

Several checks were performed to verify the quality of the data obtained with the SPMD. One of the differences between the previous analysis [15] and the present one is that, while in the previous case the analysis was performed using the total charged particle multiplicity of the detector deduced from the magnitude of the measured SPMD signals, here we simply used the total number of hit SPMD pads. The reason for using hit pads is that the correction in going from deposited charge to hits for each event and small η - ϕ segments is non-trivial. Also, the effects of two-track resolution and possible shifts of the beam position on the target during the spill were studied in detail. However all of these produced small effects which could not account for the differences observed between the data and M1 mixed events.

In order to quantify the strength of the $N_{\gamma\text{-like}}$ and N_{ch} fluctuations for various bins in ϕ and for different centrality classes, we define a quantity χ as :

$$\chi = \frac{\sqrt{(s^2 - s_1^2)}}{s_1} \quad (3)$$

where s_1 and s correspond to the rms deviations of the FFC distributions of the M1 mixed events and real data, respectively. The results are shown in Fig. 10 as a function of the number of bins in ϕ for the four different centrality classes. Qualitatively

similar results are obtained when χ is calculated using the rms deviations of the S_Z distributions. The shaded portion indicates the region of χ where s is one σ greater than the rms deviation FFC distributions for M1 events, where σ is the total error on the M1 event rms deviation. It represents the limit above which a signal is detectable. Since χ calculated from the rms deviations of the FFC distributions for data and M1 mixed events it gives the combined strength of localized fluctuations in both the photon and charged particle multiplicities. We do not present χ values calculated using M3-type mixed events. However, it is clear from the rms deviation figures that both photons and charged particles contribute to the observed fluctuations. The result shows that the strength of the fluctuations decreases as the number of bins in ϕ increases, with a strength which decreases to below detectable level (within the quoted errors) for 16 and 32 bins. It is also observed that the strength of the signal decreases with decreasing centrality for 4 and 8 bins in azimuthal angle, although the tendency is not very strong.

D. Upper limit on DCC production

It has been shown that the rms deviations of the S_Z and FFC distributions for data are very close to those of the M2 mixed events, within the quoted errors. If the DCC-like correlated fluctuations in $N_{\gamma\text{-like}}$ vs. N_{ch} were large, the rms deviations (Fig. 7 and Fig. 9) of data would have been larger compared to those of the M2 mixed events. Since this is not the case, we may extract an upper limit on the production of DCCs at the 90% confidence level following the standard procedure as discussed in Ref. [34]. This is done within the context of the simple DCC model described in section V. We give the upper limits for the two most central event classes (centrality-1 and centrality-2). From Fig. 10 it is clear that the total fluctuation is weaker for the centrality classes 3 and 4, hence the upper limits for these two classes are not presented.

The errors are assumed to have Gaussian distribution, although they are asymmetric. The larger of the asymmetric errors is conservatively used for the limit calculation. The 90% C.L upper limit contour has been calculated as $\chi + 1.28e_\chi$, where χ is calculated using Eq.(3). Here s_1 and s correspond to the rms deviations of the FFC (or S_Z) distributions for M2 mixed events and real data, respectively, and e_χ is the error in χ from the FFC (or S_Z) analysis. It may be mentioned that for the calculation of the upper limits we have assumed that the total difference in the rms values of data and M2 mixed events is due to DCC-like fluctuations only.

To relate the measured upper limit on the size of the fluctuations to a limit on DCC domain size and frequency of occurrence we proceed as follows: Within the context of the simple simulated DCC model described earlier, we obtain the rms deviations of the FFC distributions with various domain sizes in azimuthal angle (15^0 , 30^0 , \dots 180^0) and for each domain size also for different frequency of occurrence of DCC (0% to 100%). The M2 mixed events are then constructed for each of these sets of simulated events. For each set of DCC-type events of a given domain size and frequency of occurrence, the value of χ is calculated using Eq. 3, from the difference in rms deviations of the FFC distribution of the DCC event (s) and its corresponding M2 mixed event distribution ($s1$). The upper limit is set at that value of frequency of occurrence for a fixed DCC domain size at which the χ value from the DCC model matches with that of the $\chi + 1.28e_\chi$ upper limit from the experimental data. This is used to set the upper limit contour in terms of domain size and frequency of occurrence of the DCC. The results for centrality classes 1 and 2 are shown in Fig. 11. It may be mentioned that the upper limit contour set by a similar analysis of the rms values of the S_Z distributions is in agreement with those from the FFC analysis.

VII. SUMMARY

A detailed event-by-event analysis of the $\eta - \phi$ phase space distributions of the multiplicity of charged particles and photons in Pb+Pb collisions at 158-A GeV has been carried out using two different analysis methods for four different centrality classes. The results from the two analysis methods were found to be consistent with each other. The first analysis method studied the magnitude of the $N_{\gamma\text{-like}}$ versus N_{ch} multiplicity fluctuations in decreasing phase space regions. The second analysis employed the discrete wavelet transformation technique to investigate the relative magnitude of the $N_{\gamma\text{-like}}$ versus N_{ch} fluctuations in adjacent phase space regions. The results were compared to pure VENUS+GEANT simulation events and to various types of mixed events to search for and identify the

source of non-statistical fluctuations. Both analysis methods indicated fluctuations beyond those observed in simulated and M1-type mixed events for ϕ intervals of greater than 45° and which increased in strength with increasing centrality. The additional fluctuations were found to be due to uncorrelated fluctuations in both $N_{\gamma\text{-like}}$ and N_{ch} . No significant correlated fluctuations in $N_{\gamma\text{-like}}$ versus N_{ch} , a likely signature of formation of disoriented chiral condensates, were observed. Using the results from the data, mixed events, and a simple model of DCC formation, an upper limit on DCC production in 158-A GeV Pb+Pb collisions has been set.

Acknowledgments

We wish to express our gratitude to the CERN accelerator division for the excellent performance of the SPS accelerator complex. We acknowledge with appreciation the effort of all engineers, technicians and support staff who participated in the construction of this experiment.

This work was supported jointly by the German BMBF and DFG, the U.S. DOE, the Swedish NFR and FRN, the Dutch Stichting FOM, the Polish KBN under Contract No. 621/E-78/SPUB-M/CERN/P-03/DZ211/, the Grant Agency of the Czech Republic under contract No. 202/95/0217, the Department of Atomic Energy, the Department of Science and Technology, the Council of Scientific and Industrial Research and the University Grants Commission of the Government of India, the Indo-FRG Exchange Program, the PPE division of CERN, the Swiss National Fund, the INTAS under Contract INTAS-97-0158, ORISE, Grant-in-Aid for Scientific Research (Specially Promoted Research & International Scientific Research) of the Ministry of Education, Science and Culture, the University of Tsukuba Special Research Projects, and the JSPS Research Fellowships for Young Scientists. ORNL is managed by UT-Battelle, LLC, for the U.S. Department of Energy under contract DE-AC05-00OR22725. The MIT group has been supported by the US Dept. of Energy under the cooperative agreement DE-FC02-94ER40818.

-
- [1] H. Heiselberg, Phys. Rep. **351**, 161 (2001).
 - [2] M. Stephanov, K. Rajagopal, E. Shuryak, Phys. Rev. **D60**, 114028 (1999).
 - [3] A.A. Anselm, M.G. Ryskin, Phys. Lett. **B266**, 482 (1991).
 - [4] J.D. Bjorken, Int. J. Mod. Phys. **A7**, 4189 (1992).
 - [5] K. Rajagopal and F. Wilczek, Nucl. Phys. **B399**, 395 (1993); **B404**, 577 (1993).
 - [6] Zheng Huang and Xin-Nian Wang, Phys. Rev. **D49**, 4335 (1994).
 - [7] K. Rajagopal, e-print : hep-ph/9504310,
 - [8] Sean Gavin, Andreas Gocksch and Robert D. Pisarski, Phys. Rev. Lett. **72**, 2143 (1994).
 - [9] M. Asakawa, Z. Huang and X-N Wang, Phys. Rev. Lett. **74**, 3126 (1995).
 - [10] James V. Steele and Volker Koch, Phys. Rev. Lett.

- 81**, 4096 (1998).
- [11] Sean Gavin and Joseph I. Kapusta, Phys. Rev. **C65**, 054910 (2002).
- [12] Proceedings of VIII International Symposium on Very High Energy Cosmic Ray Interactions (Tokyo, Japan), 24-30 July 1994; C.M.G. Lattes, Y. Fujimoto, and S. Hasegawa, Phys. Rep. **65**, 151 (1980).
- [13] C.R.A. Augusto et al., Phys. Rev. **D59**, 1314 (1999).
- [14] T.C. Brooks et al., (Minimax Collaboration), Phys. Rev. **D55**, 5667 (1997).
- [15] M.M. Aggarwal et al., (WA98 Collaboration), Phys. Lett. **B420**, 169 (1998).
- [16] H. Appelshauser et al., (NA49 Collaboration), Phys. Lett. **B459**, 679 (1999).
- [17] M.M. Aggarwal et al., (WA98 Collaboration) Phys. Rev. **C64**, 011901(R) (2001).
- [18] M. Asakawa, H. Minakata and B. Muller, Nucl. Phys. **A 638**, 443c (1998).
- [19] H.H. Gutbrod et al., *Proposal for a Large Acceptance Hadron and Photon Spectrometer*, Preprint CERN/SPSLC 91-17, SPSLC/P260.
- [20] T.C. Awes et al., Nucl. Instr. Methods **A279**, 479 (1989).
- [21] M.M. Aggarwal et al., (WA98 Collaboration) Eur.Phys.J **C18**, 651 (2001).
- [22] M.M. Aggarwal et al., Nucl. Instr. and Methods in Phys. Res. **A424**, 395 (1999).
- [23] M.M. Aggarwal et al., (WA98 Collaboration), Phys. Lett. **B458**, 422 (1999).
- [24] W.T. Lin et al., Nucl. Instr. Methods **A389**, 415 (1997).
- [25] M.M. Aggarwal et al., (WA98 Collaboration) Phys. Rev. **C65**, 054912 (2002).
- [26] K. Werner, Phys. Rep. **C232**, 87 (1993).
- [27] R. Brun et al., GEANT3 user's guide, CERN/DD/EE/84-1 (1984).
- [28] Amara Graps, "An Introduction to Wavelets", IEEE Computational Sciences and Engineering, **2**, 50 (1995).
- [29] Zheng Huang, Ina Sarcevic, Robert Thews and Xinnan Wang, Phys. Rev. **D54**, 750 (1996).
- [30] B.K. Nandi, G.C. Mishra, B. Mohanty, D.P. Mahapatra and T.K. Nayak, Phys. Lett. **B449**, 109 (1999).
- [31] B.K. Nandi, T.K. Nayak, B. Mohanty, D.P. Mahapatra and Y.P. Viyogi, Phys. Lett. **B461**, 142 (1999).
- [32] Numerical Recipes, Cambridge Univ. Press, 1998.
- [33] B. Mohanty, Ph. D. thesis, Utkal University (2002).
- [34] G.J. Feldman and R.D. Cousins, Phys. Rev. **D57**, 3873 (1998).

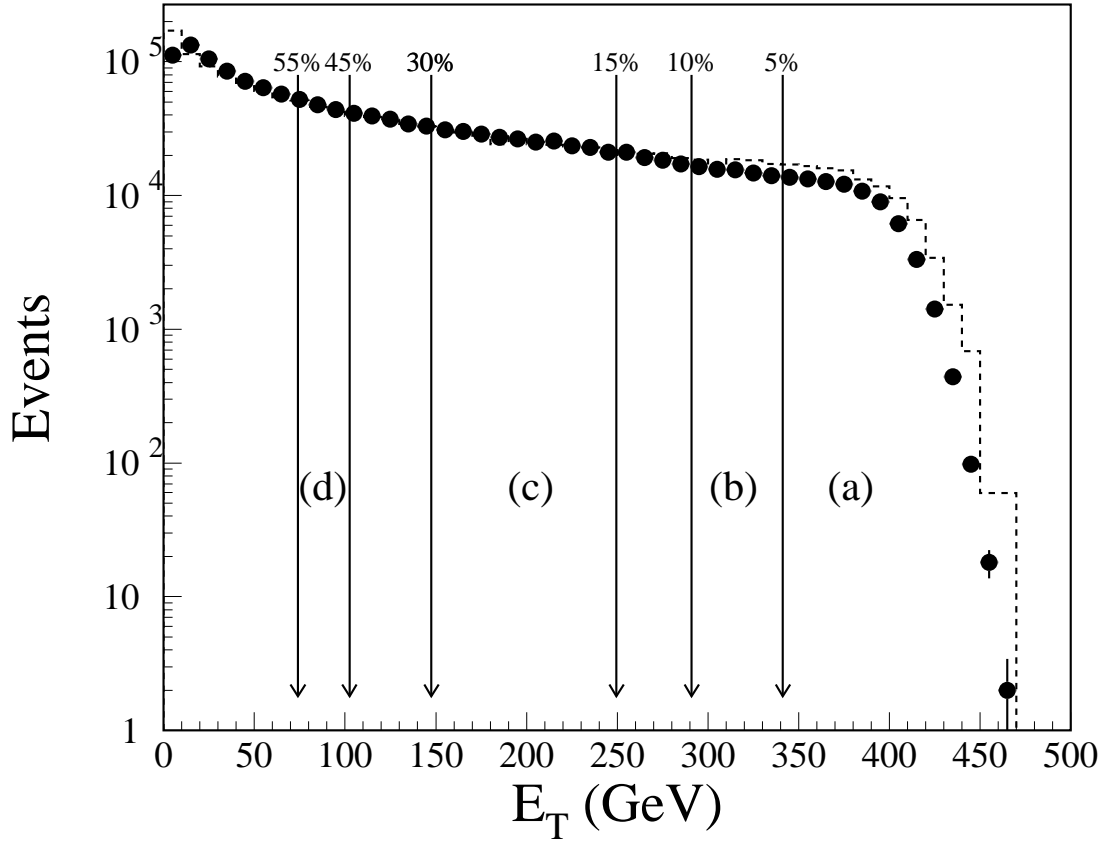


FIG. 1: The total E_T distribution (solid dots) measured in $3.5 \leq \eta \leq 5.5$ for Pb+Pb collision at 158 A GeV/c. The total E_T distribution as obtained from VENUS is also shown as dashed histogram. The E_T values corresponding to the different centrality bins used in the analysis are shown. (a) centrality-1 (0 – 5%), (b) centrality-2 (5 – 10%), (c) centrality-3 (15 – 30%), (d) centrality-4 (45 – 55%) of the minimum bias cross section as determined by selection on the measured transverse energy distribution.

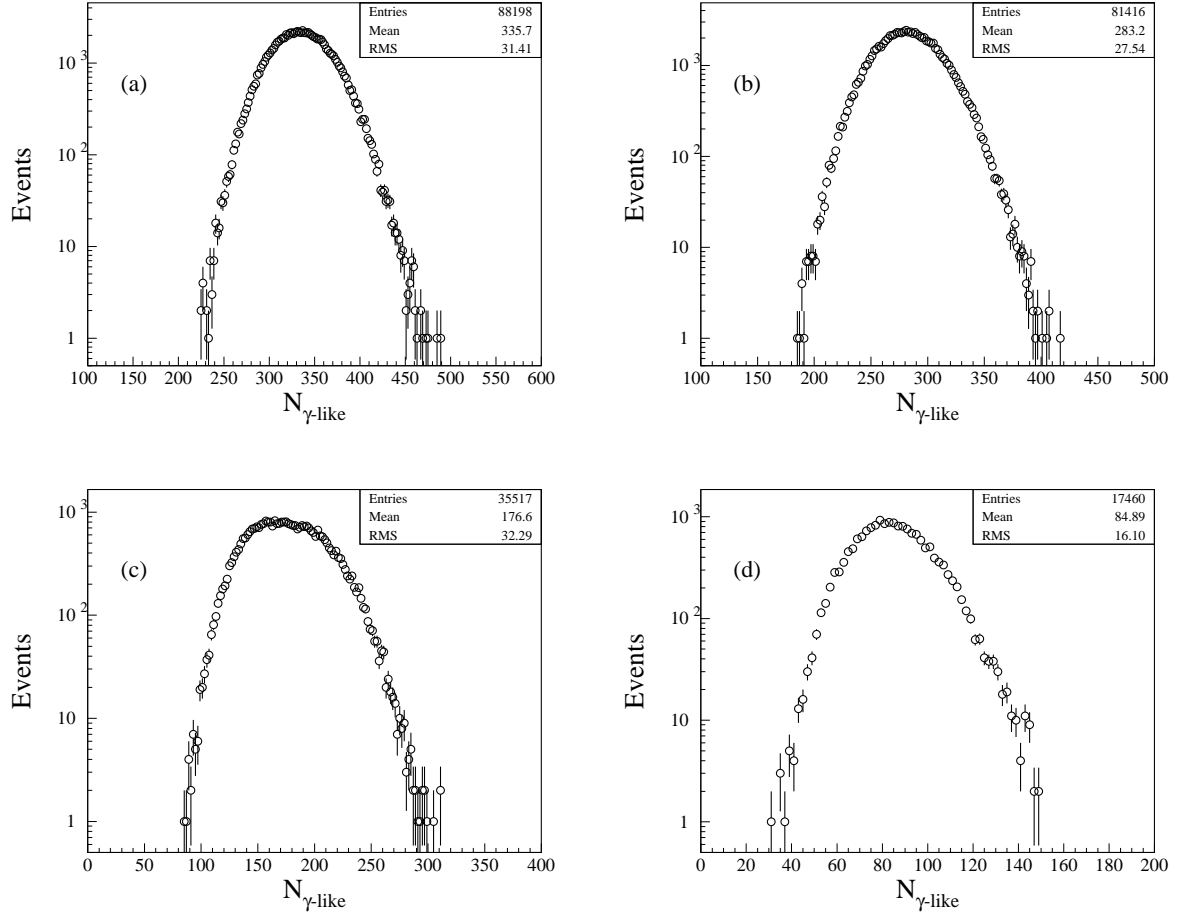


FIG. 2: The $N_{\gamma\text{-like}}$ multiplicity distributions for the four centrality selections for Pb+Pb collision at 158 A GeV/c. (a) centrality-1 (0 – 5%), (b) centrality-2 (5 – 10%), (c) centrality-3 (15 – 30%), (d) centrality-4 (45 – 55%).

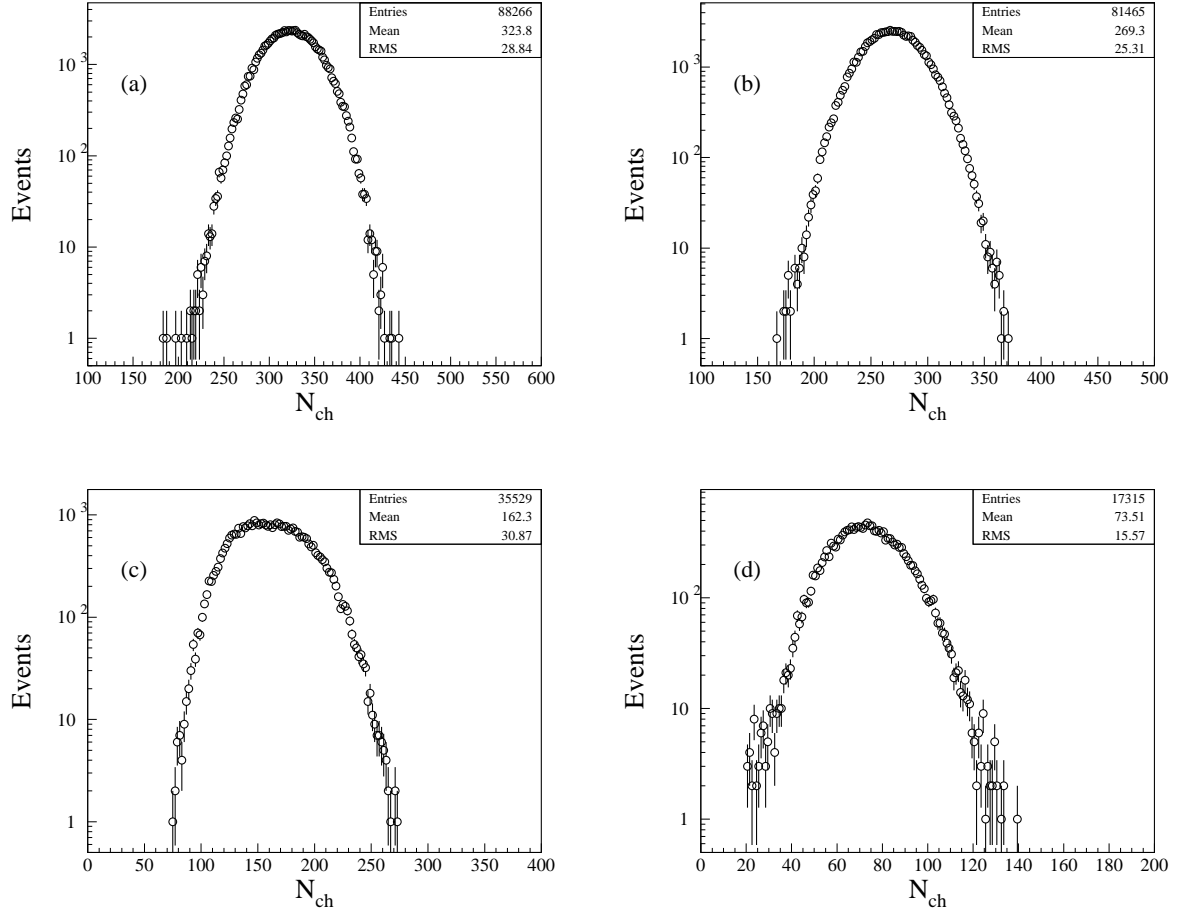


FIG. 3: The N_{ch} multiplicity distributions for the four centrality selections for Pb+Pb collision at 158 A GeV/c. (a) centrality-1 (0 – 5%), (b) centrality-2 (5 – 10%), (c) centrality-3 (15 – 30%), (d) centrality-4 (45 – 55%).

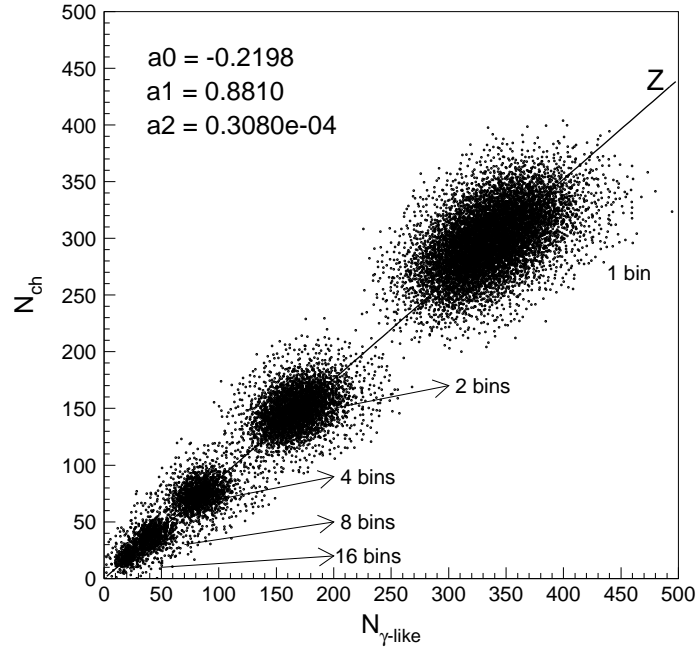


FIG. 4: The event-by-event correlation between N_{ch} and $N_{\gamma\text{-like}}$ for centrality bin=1. Overlaid on the plot is the common correlation axis (Z-axis). For the other three centrality classes, the plots are qualitatively similar.

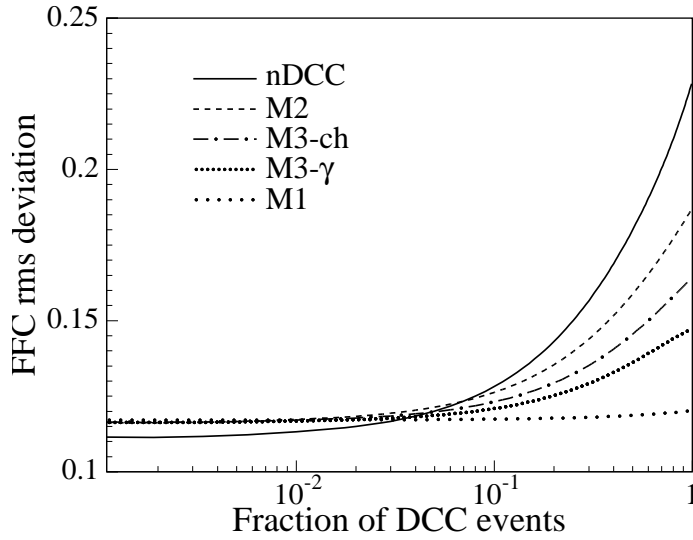


FIG. 5: The rms deviations of the FFC distributions for simulated VENUS events containing a variable fraction of localized DCC-like events with DCC extent $\Delta\phi_{DCC} = 90^\circ$, as a function of that fraction. Results are also shown for various mixed events constructed from those events.

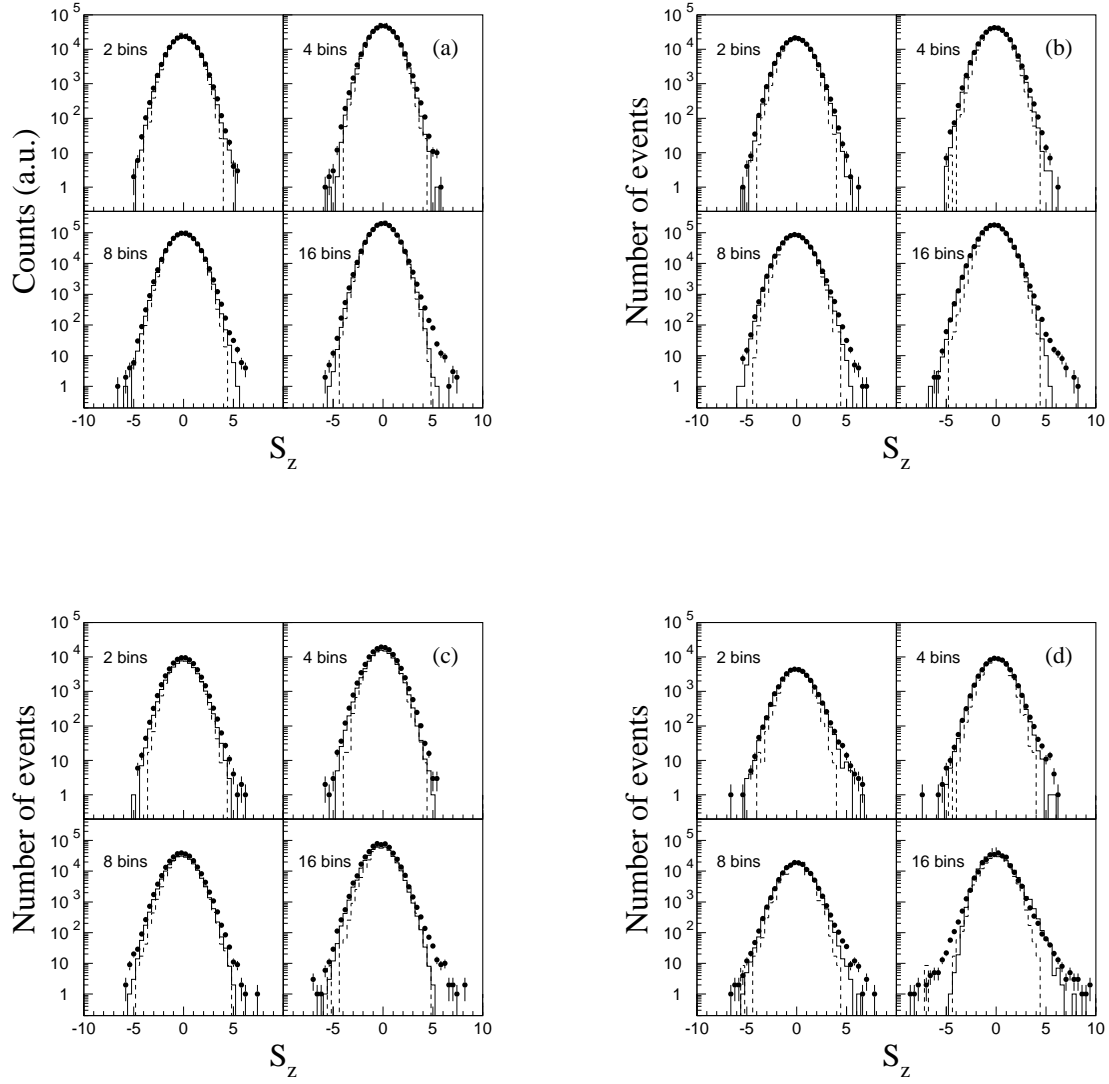


FIG. 6: The S_Z distributions for data (solid circles), mixed events (solid histogram), and simulated events (dashed histogram) for the four centrality bins (a) centrality-1 (0–5%), (b) centrality-2 (5–10%), (c) centrality-3 (15–30%), (d) centrality-4 (45–55%).

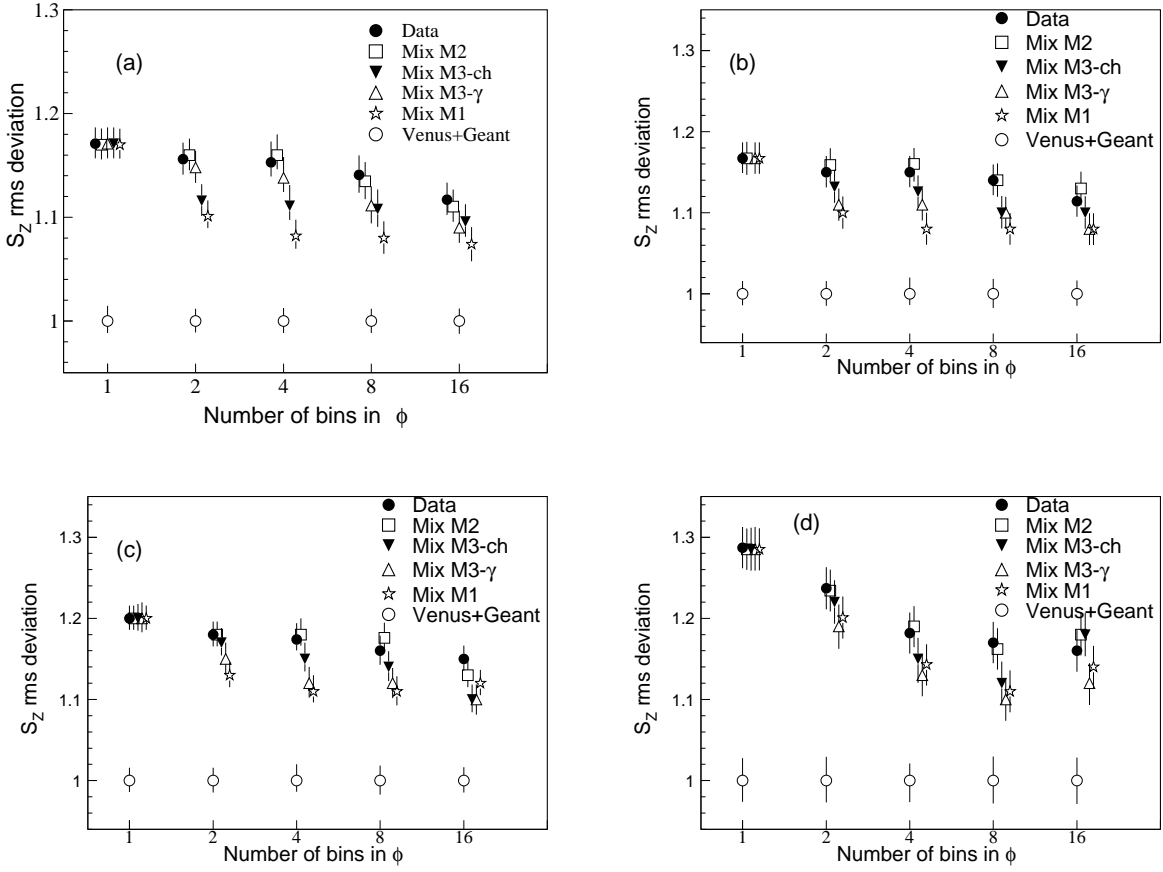


FIG. 7: The RMS deviations of the S_z distributions for data, various mixed events, and simulated events for the four centrality bins (a) centrality-1 (0 – 5%), (b) centrality-2 (5 – 10%), (c) centrality-3 (15 – 30%), (d) centrality-4 (45 – 55%).

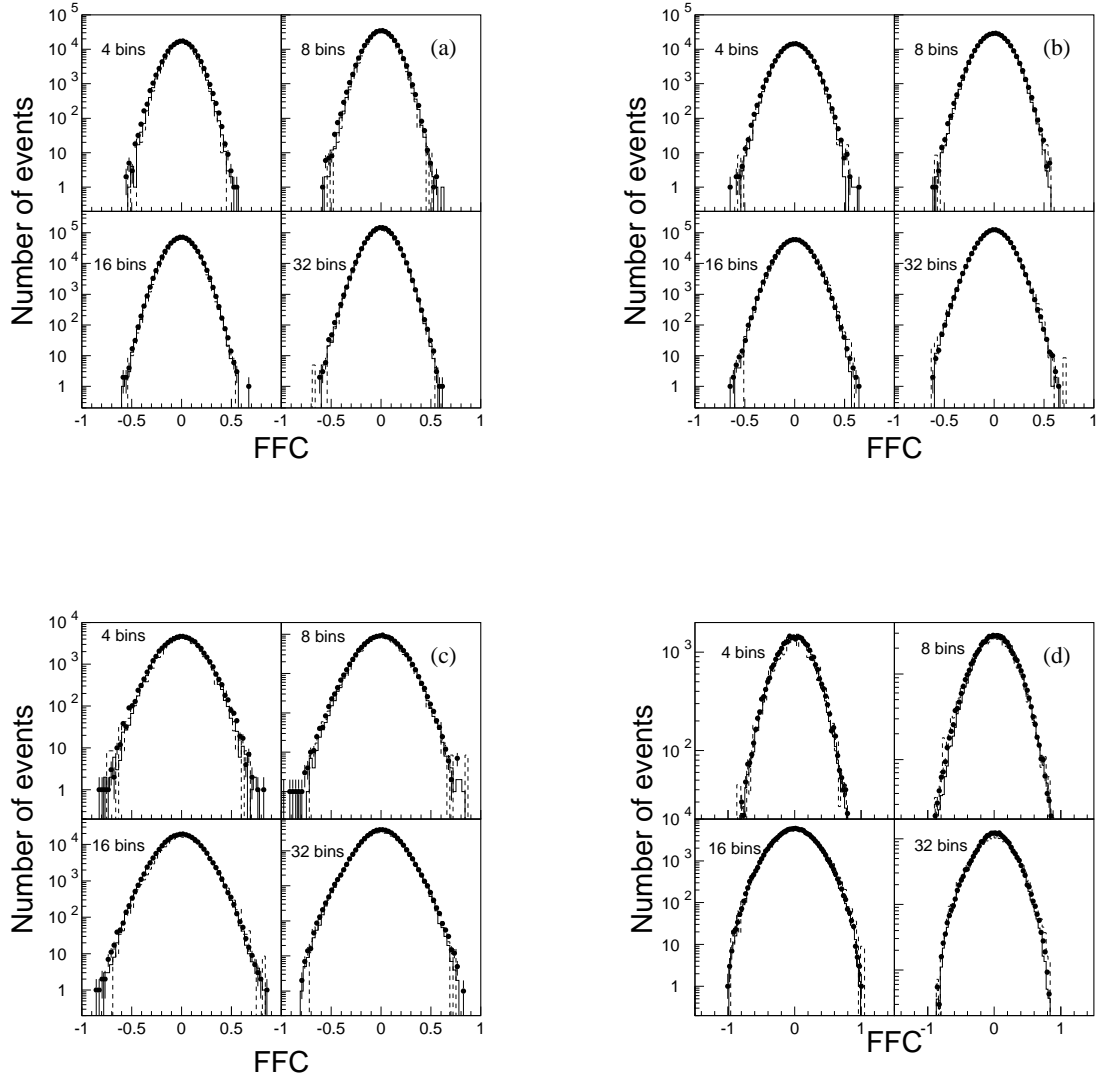


FIG. 8: The FFC distributions for data (solid circles), mixed events (solid histogram), and simulation (dashed histogram) for the four centrality bins (a) centrality-1 (0–5%), (b) centrality-2 (5–10%), (c) centrality-3 (15–30%), (d) centrality-4 (45–55%).

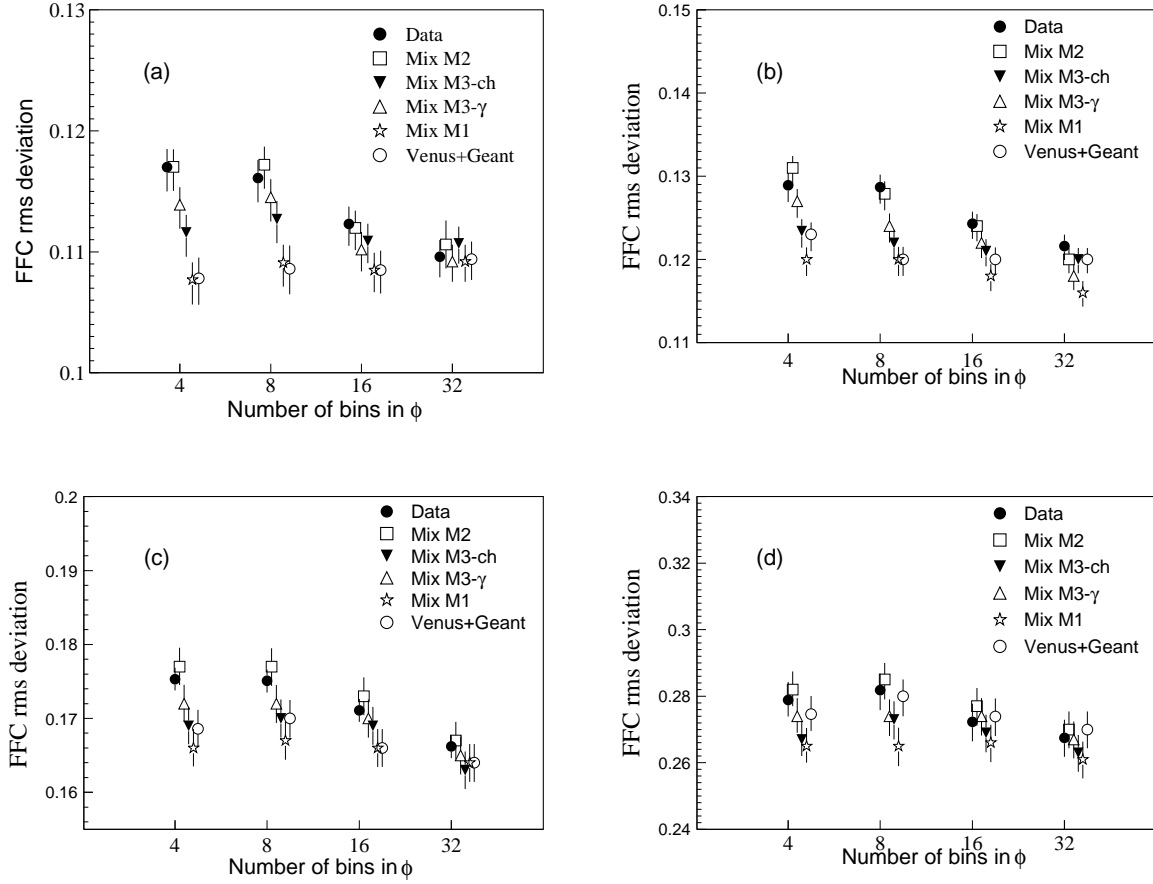


FIG. 9: The RMS deviations of the FFC distributions for data, various mixed events, and simulation for the four centrality bins (a) centrality-1 (0 – 5%), (b) centrality-2 (5 – 10%), (c) centrality-3 (15 – 30%), (d) centrality-4 (45 – 55%).

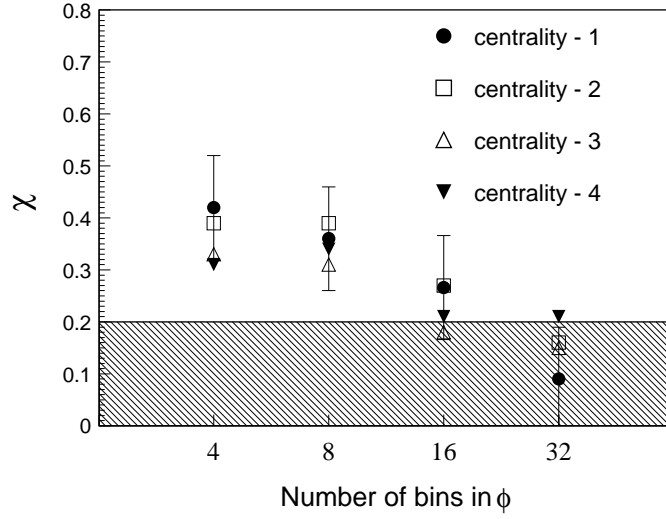


FIG. 10: The fluctuation strength parameter for the four centrality classes. Centrality-1 corresponds to the 5% most central, centrality-2 corresponds to 5 – 10%, centrality-3 corresponds to 15 – 30% and centrality-4 corresponds to 45 – 55% of the minimum bias cross section as determined by selection on the measured transverse energy distribution. The error bars are shown only on the centrality-1 selection for clarity of presentation. The errors are similar for the other centralities.

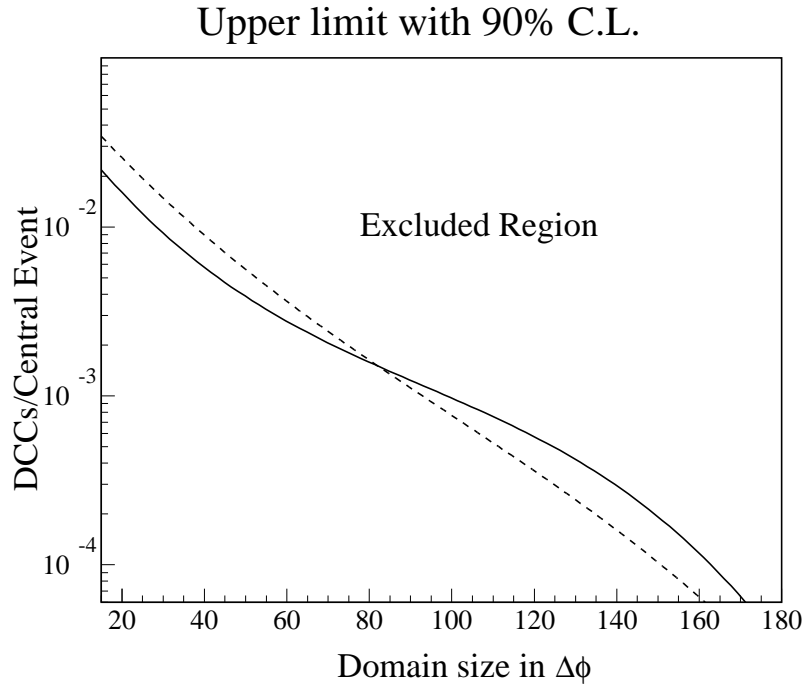


FIG. 11: The 90% confidence level upper limit on DCC production for central Pb+Pb collision at 158· A GeV/c, as a function of the DCC domain size in azimuthal angle within the context of a simple DCC model and the measured photon and charged particle multiplicities in the interval $2.9 < \eta < 3.75$. The solid line corresponds to data from the top 5% and dashed line to top 5 – 10% of the minimum bias cross section as determined by selection on the measured transverse energy distribution.